Low-temperature hydrogenation of dimethyl oxalate to ethylene glycol *via* ternary synergistic catalysis of Cu and acid−base sites

Guoqing Cui[a], Xiaoyu Meng[a], Xi Zhang[a], Wenlong Wang[a], Sailong Xu[a], Yingchun Ye[b], Kangjian Tang[b], Wanmin Wang[b], Junhua Zhu[b,*], Min Wei[a,*], David G. Evans[a], Xue Duan[a]

[a] *State Key Laboratory of Chemical Resource Engineering, Beijing Advanced Innovation Center for Soft Matter Science and Engineering, Beijing University of Chemical Technology, Beijing, 100029, PR China*
[b] *SINOPEC Shanghai Research Institute of Petrochemical Technology, Shanghai, 201208, PR China*

ABSTRACT

Metal-support synergistic catalysis plays a crucial role in heterogeneous reaction processes from viewpoint of both fundamental research and practical applications. Herein, a series of Cu-based nanocatalysts were prepared by virtue of topotactic structure transformation from CuMgAl-layered double hydroxide (CuMgAl − LDH) precursors. Various *in situ* investigations including XRD, XPS, EXAFS and FTIR demonstrate that the structural transformation of CuMgAl − LDH results in well-dispersed Cu nanoparticles (metallic Cu° as the single species) supported on mixed metal oxides (MgO and Al_2O_3, denoted as Cu/MMO). The optimal catalyst (Cu/MMO − S3) exhibits an excellent catalytic performance toward hydrogenation of dimethyl oxalate (DMO) to ethylene glycol (EG) (yield: 94.4%) at an exceptionally low operation temperature (438 K). This is, to the best of our knowledge, at least 30—40 K lower than normally accepted temperature for Cu-based catalysts (above 473 K). Structure − property correlation investigations were performed *via in situ* FTIR, N_2O pulse chemisorption, NH_3−TPD and CO_2−TPD, and the results revealed that a ternary synergistic catalysis of Cu and acid − base sites makes a predominant contribution: Lewis acid sites (Al^{3+}) and medium-strong basic sites ($Mg^{2+} − O^{2−}$ pair) of supports serve as active sites for adsorption of polarized $C=O/C−O$ group in DMO molecule; while H_2 undergoes dissociation adsorption on Cu° site. This precise control over metal and acid − base sites based on LDHs precursor approach would lead to new possibilities in rational design and preparation of heterogeneous catalysts for hydrogenation of $C=O/C−O$ group.

1. Introduction

Owing to the shrinking oil resources and increasing environmental issue, considerable attention has been focused on highly-efficient and environmentally-friendly utilization of coal resources to obtain high value-added chemical products [1]. One of the most encouraging ways is C1 chemistry with high atom economy and low waste emission, which has drawn extensive interest from both fundamental research and industrial application [2]. Catalytic syngas (CO + H_2) conversion plays a pivotal role in C1 chemistry, which provides the most versatile reaction system to produce alternatives of petroleum-derived fuels and valuable chemicals [3,4]. For instance, syngas conversion *via* vapor-phase hydrogenation of dimethyl oxalate (DMO) to ethylene glycol (EG), serves as a promising route (Scheme 1) for the production of polyester fibers, antifreeze, solvent, *etc* [5,6]. This reaction is industrially carried out with the assistance of heterogeneous transition-metal Cu − Cr catalysts [7] or silica supported Cu catalysts [8]. However, this catalytic process normally suffers from huge energy consumption and rigorous reaction conditions (*e.g.*, reaction temperature: ˜493 K; pressure: ˜3.0 MPa; a large H_2/DMO molar ratio of ˜80 *etc*.), for the purpose of achieving favorable conversion, selectivity and lifespan. Therefore, how to develop highly-efficient and low-cost catalysts based on structure design and synthesis exploration, so as to attain vapor-phase hydrogenation of DMO to EG under mild reaction conditions, still remains a big challenge.

Copper-based catalysts have been intensively applied in hydrogenation/hydrogenolysis of carbon-oxygen ($C=O/C−O$) bonds (*e.g.*, esters, alcohols and CO_2), owing to their high selectivity toward hydrogenation of carbon-oxygen bonds but inactivity for carbon-carbon bonds [9–11]. Recently, Cu/SiO_2 catalysts have shown excellent catalytic performance for DMO vapor-phase hydrogenation, serving as a promising substitution for traditionally used toxic Cu–Cr catalysts

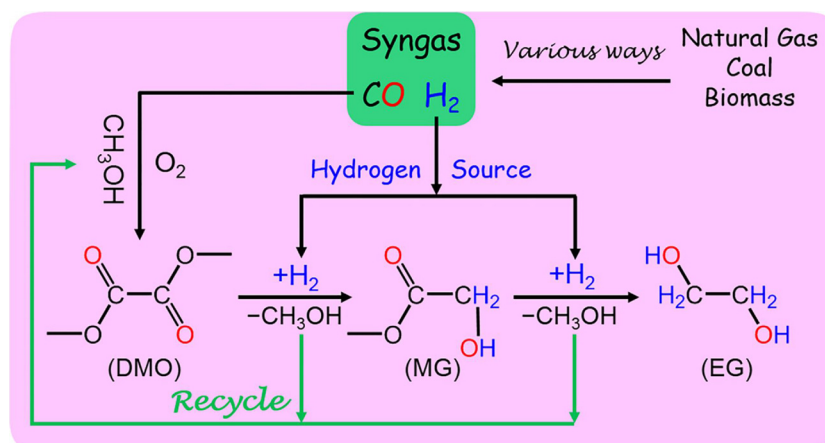**Scheme 1.** Proposed reaction routes from syngas to ethylene glycol (EG) in C1 chemistry way.

[8,12,13]. A synergistic catalysis between Cu^+ sites and $Cu°$ sites has been reported for DMO conversion in Cu/SiO_2 catalytic systems, in which Cu^+ acts as adsorption site for C=O/C−O bond while $Cu°$ contributes to hydrogen dissociation [10,14–16]. Several routes have been adopted (*e.g.*, noble or rare-earth metals co-catalysts) to achieve a suitable $Cu^+/Cu°$ species balance and enhanced catalytic behavior [17–21]. Although much progress has been made in this area, seldom study has been focused on metal-support interactions and how to improve catalytic performance *via* tuning metal-support interactions. Acid − base property of supports has been widely recognized as a key factor in the promotion of catalytic hydrogenation processes, especially for activation adsorption of C=O/C−O bonds. It has been reported that acidic sites of supports participate in catalytic process *via* polarizing and activating C=O bond while basic sites interact with π* acceptor orbital of C=O bond to facilitate hydrogenolysis of C−O bond [22–25]. According to these findings of previous studies, it would be a promising strategy to design and prepare Cu catalysts with cooperative catalysis between metal and acid − base sites from supports, so as to achieve high-efficiency hydrogenation of DMO to EG.

Recently, researchers have reported the preparation of supported metal catalysts based on structure topotactic transformation process of layered double hydroxides (LDHs) precursors [26–28]. A reduction treatment of LDHs precursors in a hydrogen atmosphere would result in highly-dispersed metal nanoparticles supported on mixed metal oxides matrix. The most attractive characteristic of this method lies in a facile tuning over metal-support interactions (*e.g.*, electronic metal-support interaction, metal/support acid − base interaction). Especially, the quantity and strength of acid − base structure of supports can be efficiently modified *via* precisely controlling the topotactic transformation parameters (*e.g.*, reduction atmosphere, temperature, heating rate, *etc.*) of LDH precursors. Our previous work has shown that the catalytic behavior of supported Ni nanoparticles (derived from NiAl − LDHs precursor) toward dehydrogenation of alcohols is largely enhanced *via* tuning the synergistic catalysis between Ni° site and acid − base sites [29]. This specific property of LDHs precursors further inspires us to explore supported Cu catalysts by means of LDHs approach: a precise control over synergistic catalysis between copper species and acidity/basicity of supports would lead to a strengthened activation of C=O/C−O bonds.

Herein, we report the synthesis of Cu-based nanocatalysts on the basis of topotactic structure transformation of CuMgAl − LDHs precursors *via* a two-step procedure: a careful calcination of LDHs precursors at various temperatures to obtain mixed metal oxides (denoted as CuMgAl − MMO), followed by a reduction treatment process (denoted as Cu/MMO). The resulting supported Cu catalysts are featured with a high dispersion of Cu nanoparticles (6–9 nm) and configurable acid − base sites of support (MgO and Al_2O_3). Notably, the optimal

catalyst Cu/MMO − S3 exhibits an excellent catalytic performance for DMO hydrogenation to EG (conversion: 98.2%; selectivity: 96.1%) at an exceptionally low reaction temperature (438 K), which is at least 30–40 K lower than normally accepted temperature for Cu-based heterogeneous catalysts (above 473 K). A combination investigation (*in situ* XRD, *in situ* XPS, *in situ* EXAFS and *in situ* FTIR) confirms that calcination-reduction treatment leads to the transformation from CuMgAl − LDHs to well-dispersed Cu nanoparticles with metallic Cu° as the single species. *In situ* FTIR of pyridine, NH_3 − TPD and CO_2 − TPD demonstrate the coexistence of medium-strong basic sites ($Mg^{2+} − O^{2-}$ pair) and Lewis acid sites (Al^{3+}) in abundance. In addition, *in situ* FTIR of DMO and H_2 − TPD give direct evidences that the acid − base sites of supports serve as active sites for adsorption of polarized C=O/C−O group while H_2 molecule undergoes dissociation adsorption on Cu° sites. The cooperative effect of Cu°/acid − base sites accounts for the exceptional catalytic behavior toward DMO vapor phase hydrogenation at such a low temperature. This work provides a paradigm for the hydrogenation of C=O/C−O under mild conditions by virtue of metal-support synergistic catalysis, and the insights on structure − property correlation can be extended to other fatty ester heterogeneous hydrogenation reactions.

2. Experimental

2.1. Materials

All the chemicals and reagents (analytical grade) were obtained from Sigma-Aldrich, including: Na_2CO_3, $NaOH$, $Cu(NO_3)_2·3H_2O$, $Mg(NO_3)_2·6H_2O$, $Al(NO_3)_3·9H_2O$, dimethyl oxalate, methyl glycolate, ethylene glycol, n-butanol, methanol, ethanol. Deionized water with an electrical conductivity $< 10^{-6}$ S·cm^{-1} was used in all experimental processes.

2.2. Catalyst synthesis

2.2.1. Synthesis of CuMgAl − LDH precursors

CuMgAl − LDH precursors were synthesized by the separate nucleation and aging steps method (SNAS) reported by our group [30]. In a typical procedure, $Cu(NO_3)_2·3H_2O$, $Mg(NO_3)_2·6H_2O$, $Al(NO_3)_3·9H_2O$ with a molar ratio of $Cu^{2+}:Mg^{2+}:Al^{3+} = 1:1:1$ were dissolved in deionized water (100 mL) to give solution A (total cationic concentration: 1.00 M). NaOH and Na_2CO_3 were dissolved in water (100 mL) to give solution B ($[CO_3^{2-}] = 2.0 [M^{3+}]$ and $[OH^-] = 1.8 ([M^{2+}] + [M^{3+}])$). Solution A and B were mixed together simultaneously in a colloid mill (rotating rate of 3000 RPM for 3.0 min), followed by aging in a sealed Teflon autoclave at 373 K for 12 h. The resulting precipitate was thoroughly washed *via* centrifugation and then dried at 333 K for

12 h (denoted as CuMgAl − LDH).

2.2.2. Synthesis of Cu/MgO/Al₂O₃ catalyst

Typically, CuMgAl − LDH sample (1.00 g) was calcined in air for 4.0 h at 673 K, 773 K, 873 K, 973 K, and 1073 K, respectively, and then cooled down to room temperature to obtain MMO samples (from CuMgAl − MMO − S1 to CuMgAl − MMO − S5). Subsequently, the as-synthesized samples of Cu/MMO were tableted, crushed and sieved to 40–60 meshes, and then reduced in a H₂/N₂ (1/9, v/v) stream for 4.0 h at 573 K (heating rate: 2 K·min⁻¹). The as-obtained products, denoted as Cu/MMO (from Cu/MMO − S1 to Cu/MMO − S5), were cooled down to room temperature in a nitrogen stream for subsequent catalytic evaluations.

2.2.3. Synthesis of Cu/MgO, MgO − Al₂O₃ and Cu/Al₂O₃

These three samples, as control catalysts, were prepared by a similar coprecipitation method. For the preparation of Cu/MgO, an aqueous solution (100 mL) of NaOH (0.5 mol L⁻¹) and Na₂CO₃ (0.5 mol L⁻¹) was added dropwise into a solution (1.0 mol L⁻¹) containing Cu(NO₃)₂·3H₂O and Mg(NO₃)₂·6H₂O, with the pH value of 9 ± 0.2. In order to give a parallel comparison, a similar treatment process (aging, calcination and reduction) as Cu/MMO − S3 was performed to obtain Cu/MgO, Cu/Al₂O₃ and MgO − Al₂O₃ as reference samples.

2.3. Characterizations

In situ XRD patterns were measured by Rigaku XRD − 6000 diffractometer with a sample cell connected to a gas mass flow controllers, by using Cu Kα radiation (λ = 0.15418 nm, 40 kV, 40 mA) at a scanning rate of 5°·min⁻¹. Every CuMgAl − MMOs sample was firstly reduced in a H₂/He (1/9, v/v; 50 mL min⁻¹) stream at 573 K for 4.0 h, followed by flushing (50 mL min⁻¹) and cooled to 438 K (in accordance with reaction temperature) with a He stream for 1.0 h. Specific surface area was studied by Brunauer − Emmett − Teller (BET) methods on a Micromeritics ASAP 2020 Instrument. High-resolution transmission electron microscopy (HRTEM) was conducted on a JEOL JEM − 2010 (accelerating voltage: 200 kV). Chemical compositions of samples were measured on a Shimadzu ICPS − 7500 inductively coupled plasma–atomic emission spectrometer (ICP − AES). Temperature-programmed reduction of hydrogen (H₂ − TPR) was measured by using a Micromeritics ChemiSorb 2920 equipped with an on-line mass spectrometry (MS) and a thermal conductivity detector (TCD). In a typical procedure, the sample (100 mg) was sealed in a quartz tube and pretreated in a Ar flow (473 K, 2 h), followed by a reduction process in a H₂/Ar stream (1/9, v/v; 50 mL min⁻¹) at a rate of 10 K·min⁻¹ from 323 K to 1173 K.

The dispersion of Cu and specific surface area of metallic Cu were determined by N₂O chemisorption and hydrogen pulse reduction method (N₂O titration) on a Micromeritics Autochem II 2920 equipped with a TCD and an on-line mass spectrometry (MS). Briefly, after pretreatment with He flow at 473 K for 2.0 h, the sample (100 mg) was reduced in a H₂/Ar flow (1/9, v/v; 50 mL min⁻¹) at 573 K for 2 h, and the corresponding hydrogen consumption (denoted as X) was detected. Afterwards, the sample was flushed with high purity Ar for 1.0 h and cooled down to 323 K. Subsequently, a pure flow of N₂O was induced at a rate of 50 mL min⁻¹ for 2.0 h, guaranteeing a complete oxidization of surface Cu atoms to Cu₂O. Then successive pulses of high-purity H₂ were introduced at 573 K to reduce surface Cu₂O to metallic Cu, with Ar as carrier gas (50 mL min⁻¹). The volume of consumed hydrogen was obtained by subtracting the sum of residual unsaturated hydrogen pulses from the total hydrogen injection volume (denoted as Y). The dispersion of metallic Cu (D%, Eq. 1), was obtained according to N₂O chemisorption value:

$$D(\%) = \frac{2 \times Y}{X} \times 100 \qquad (1)$$

The surface area of surface Cu species per gram catalyst (S (m²·g$_{cat}$⁻¹), Eq. 2) was calculated as follows:

$$S = \frac{2 \times N_A \times Y}{X \times 1.4 \times 10^{19} \times M_{Cu} \times Wt_{Cu}\%} = \frac{1353 \times Y}{X \times Wt_{Cu}\%} \qquad (2)$$

Where M_{Cu}, $Wt_{Cu}\%$ and N_A are the molecular weight of Cu, mass percentages of copper species, Avogadro's constant, respectively, 1.4×10^{19} is the number of copper atoms per square meter [31].

Temperature-programmed desorption of CO₂ (CO₂ − TPD) and NH₃ (NH₃ − TPD) were carried out on an AutoChem II 2920 Chemisorption equipment with a TCD and an on-line MS. The sample (100 mg) was reduced at 573 K for 2 h in H₂/Ar atmosphere (1/9, v/v; 50 mL min⁻¹), followed by purging with a high purity He flow (50 mL min⁻¹) for 2.0 h at 583 K. When the temperature decreased to 323 K, CO₂ (or NH₃) was introduced until saturation, followed by purging He (50 mL min⁻¹) for 90 min to remove physisorbed CO₂ (or NH₃). Finally, the sample was heated from 323 K to 873 K at a rate of 10 K min⁻¹, and the released CO₂ (or NH₃) was monitored by a mass spectrometer.

In situ X-ray photoelectron spectra (XPS) and X-ray excited Auger electron spectra (XAES) were carried out on an AXIS ULTRA DLD spectrometer with Al Kα resource ($h\nu$ = 1486.6 eV) equipped with a catalytic reaction chamber (allowed 3 MPa and 573 K). To investigate the Cu chemical state, the sample was compressed into a thin disk and reduced in a H₂/Ar flow (1/9, v/v; 50 mL min⁻¹) flow at 573 K for 4.0 h in a reaction chamber. Afterwards, the sample was carefully transferred into the XPS measurement chamber under high vacuum conditions. For investigating the evolution of copper species during the reaction process, DMO solution was fed into the pretreatment chamber by pump within H₂/Ar (1/9, v/ v; 50 mL min⁻¹) at 438 K and 2.0 MPa for 24 h after the sample was reduced at 573 K for 2 h. Subsequently, the sample was transferred into the XPS measurement chamber under high vacuum conditions. The XPS and XAES spectra of metallic Cu, Cu₂O and CuO were recorded for reference. The contaminated carbon C 1s signal (284.6 eV) was used to calibrate binding energy.

In situ extend X-ray absorption fine structure spectroscopy (EXAFS) at the Cu K-edge was measured at the beamline 1W1B of the Beijing Synchrotron Radiation Facility (BSRF), Institute of High Energy Physics (IHEP), and Chinese Academy of Sciences (CAS). The sample was pressed into thin sheet on a reactor cell equipped with polyimide windows, and then reduced in a H₂/He flow (1/9, v/v; 50 mL min⁻¹) at 573 K, followed by purging He (50 mL min⁻¹) for 1.0 h. Afterwards, the reduced sample was cooled slowly to 438 K (the reaction temperature) in a He stream, for the measurement of EXAFS spectra. Fourier transform of EXAFS spectra were performed in a K-range from 3.0 to 12.8 Å⁻¹. The IFFEFIT 1.2.11 date analysis package (Athena, Artemis, Atoms, and FEFF6) was used for analysis and fitting.

In situ FTIR spectra of pyridine, CO and DMO solution were recorded by adding 64 scans for the sample at a resolution of 4.0 cm⁻¹ for all samples, using a Tensor 27 (Bruker Company) instrument with a modified transmission FTIR cell. The FTIR cell was equipped with KBr windows and inlet/outlet system with mass flow controllers, thermocouples and heater to monitor and control temperature. The sample (20 mg) was pressed into a self-supporting wafer, followed by activation in 10% H₂/He at 573 K for 2.0 h. For *in situ* FTIR measurements for CO and pyridine, the reduced sample was cooled to 300 K in a He flow to obtain the background baseline signal, followed by the introduction of CO/He (1/9, v/v; 50 mL min⁻¹) or pyridine until saturation. Afterwards, the sample was evacuated at different temperature for 30 min for the collection of infrared signal *vs.* the reference signal. For *in situ* FTIR spectra of DMO solution, the sample after reduction was cooled down to 303 K in a He flow, vacuumed to remove the gaseous species. Then, a certain amount of DMO solution was carefully evaporated and pulsed into the thin cell for 1.0 h, followed by evacuation to remove weakly-adsorbed DMO; and spectra were measured at every minute at different temperature.
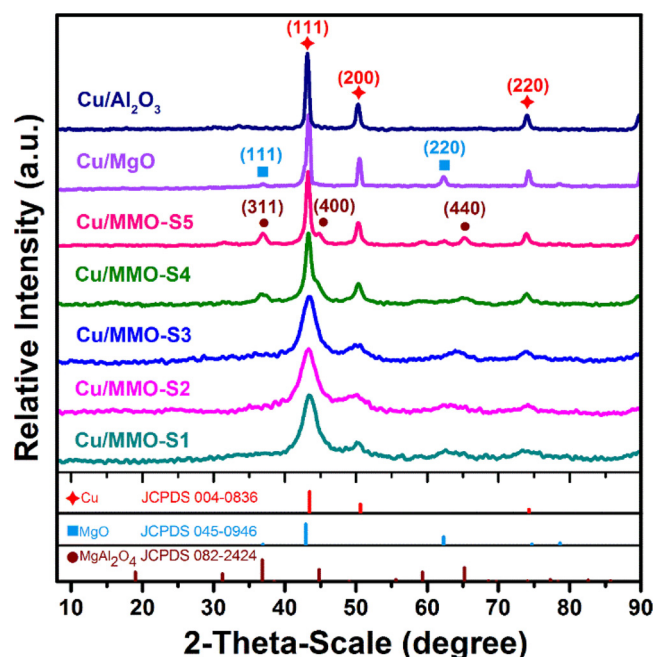
Fig. 1. *In situ* XRD patterns of series Cu/MMO samples, Cu/MgO and Cu/Al₂O₃ at the reduction temperature of 573 K.

2.4. Catalytic evaluations

Vapor-phase hydrogenation of DMO was performed in a micro-reaction system over a stainless steel fix-bed reactor (inner diameter: 8.0 mm; length: 600 mm), equipped with a thermocouple for the control of reaction temperature. Briefly, 2.0 g of catalyst (40–60 meshes) was loaded in the middle zone of reaction tube, reduced at 573 K for 4.0 h by H_2/N_2 (1/9, v/v; 99.99% purity) using a mass flow controller of Brooks Co. (50 mL min^{-1}). After cooling to the reaction temperature, a feedstock of DMO (99.9% purity solid) in methanol solvent (1/9, wt/wt) was injected into the reactor through a high-pressure pump (Lab Alliance Series III pump) and vaporized (423 K) with a certain pressure, H_2/DMO molar ratio and weight liquid hourly space velocity (WLHSV). The products were collected into a cold trap (100 mL, constant temperature 280 K), and then analyzed on a gas chromatograph (GC-2014C, Shimadzu Company) furnished with a DB − WAX − UI capillary column (Agilent Technologies Company, 30m × 0.25 mm × 0.25 mm) and a flame ionization detector (FID). The main by-products including dimethyl oxalate, methyl glycolate, ethylene glycol, *n*-butanol, methanol, ethanol, methyl methoxyacetate, were determined quantitatively by internal standard method (*n*-butanol). The conversion and product selectivity were calculated according to the following equations:

$$Conversion\,(\%) = \left(1 - \frac{Molar\ amount\ of\ feed\ after\ reaction}{Total\ molar\ amount\ of\ feed}\right) \times 100\% \quad (3)$$

$$Selectivity\,(\%) = \frac{Molar\ amount\ of\ one\ product}{Total\ molar\ amount\ of\ feed\ converted} \times 100\% \quad (4)$$

The initial turn over frequency (TOF) of DMO to EG was measured at a low DMO conversion (below 20%). The TOF value indicates the moles of DMO converted per hour by per mole metal on catalyst surface (mol-DMO mol-metalsurf^{-1} h^{-1}, for short h^{-1}), which is calculated according to the following equation:

$$TOF\,(h^{-1}) = \frac{Molar\ amount\ of\ DMO\ converted}{Molar\ amount\ of\ metal\ on\ catalyst\ surface\ \times\ reaction\ time} \quad (5)$$

3. Results and discussion

3.1. Structural and morphological investigations

The CuMgAl − layered double hydroxides (CuMgAl − LDH) precursors were prepared by using separate nucleation and aging steps (SNAS) developed in our group [30], whose and XRD patterns (Fig. S1a) exhibited several characteristic reflections at 2θ 11.7° (003), 23.5° (006) and 34.9° (012), same to a typical CuMgAl − CO₃−LDH phase [32]. After a calcination treatment in air at 673 K, 773 K, 873 K, 973 K and 1073 K, respectively, a structural transformation from CuMgAl − LDH to mixed metal oxides occurs (denoted as sequential sign from CuMgAl − MMO − S1 to CuMgAl − MMO − S5). The XRD spectra of these CuMgAl − MMO samples (Fig. S1, b–f) display three broad reflections centered at 2θ 35.8°, 43.7° and 63.8°, attributed to a mixed phases of CuO (JCPDS 045 − 0937) and low-crystallinity MgO (JCPDS 045 − 0946), accompanied by the disappearance of LDH reflections. No reflections of Al₂O₃ are detected, implying its amorphous phase. As the calcination temperature is above 973 K (CuMgAl − MMO − S4 and CuMgAl − MMO − S5), three weak reflections at 2θ 36.9°, 44.9° and 65.2° are observed, which are indexed as (311), (400) and (440) of CuAl₂O₄ (JCPDS 099 − 0098) and/or MgAl₂O₄ phase (JCPDS 082–2424) [33]. In addition, CuO − MgO and CuO − Al₂O₃, as reference samples, were synthesized by traditional co-precipitation method and annealed under the same conditions, which showed similar phase of CuO, MgO and Al₂O₃ (Fig. S1, Table S1).

Subsequently, CuMgAl − MMO samples were reduced in a H_2/Ar (1/9, v/v) atmosphere at 573 K to obtain Cu nanoparticles supported on MMO matrix (denoted as sequential sign from Cu/MMO − S1 to Cu/MMO − S5). *In situ* XRD technique was employed to identify the phase transformation after the reduction process, in order to avoid possible oxidation of Cu nanoparticles. For all these Cu/MMO samples (Fig. 1), a strong reflection at 2θ 43.3° and two weak ones at 50.4° and 74.1° are observed, which are assigned to the (111), (200) and (220) lattice plane of metallic Cu (JCPDS 004 − 0836). From Cu/MMO − S1 to Cu/MMO − S4, the peak intensity enhances gradually with the decrease of full width at half maxima (FWHM) of metallic Cu, and the particle size of Cu increases from 4.5 to 6.1 nm progressively calculated by the Debye-Scherrer equation (Table 1); while a significant increment to 8.3 nm is observed for the Cu/MMO − S5 sample. As reference samples, XRD pattern of Cu/MgO shows an fcc Cu and a cubic MgO phase while Cu/Al₂O₃ only displays a Cu phase, with Cu particle size of 9.1 nm and 9.3 nm, respectively.

TEM measurements were carried out to study the structure and morphology features of these samples. HRTEM images (Fig. 2) of five Cu/MMO samples and reference samples (Cu/MgO and Cu/Al₂O₃) show that Cu nanoparticles are uniformly immobilized on the surface of supports with a high density, whose lattice fringe of 0.209 nm (Fig. 2, A2 − E2 and Fig. S2, A2 − B2) corresponds to the (111) plane of fcc Cu phase revealed by fast Fourier transform (FFT). Notably, the mean particle size of Cu nanoparticles in Cu/MMO samples increases gradually from 5.2 nm to 8.8 nm (Fig. 2, A1–E1), which are smaller than that in Cu/MgO (9.4 nm) and Cu/Al₂O₃ (9.7 nm) samples (Fig. S2, A1–B1), in approximate agreement with the result of *in situ* XRD (Table 1). Moreover, the Cu dispersion (D_{Cu}) and surface area of Cu (SA_{Cu}) were measured by classic N_2O chemisorption (Table 1), both of which display an increase from Cu/MMO − S1 to Cu/MMO − S3, but decrease from Cu/MMO − S3 to Cu/MMO − S5. The results illustrate the influence of calcination temperature (the first step of preparation process) on the evolution of Cu species: a moderate calcination temperature (*e.g.*, 873 K) leads to a high dispersion of Cu nanoparticles with a large surface area; whilst an exorbitant temperature (≥973 K) induces sintering of Cu to some extent.

Table 1
Physicochemical Properties of Various Samples.

Catalyst	BET surface area $(m^2 \cdot g^{-1})$	Cu species content [a] (wt.%)	Cu crystallite size [b] (nm)	Mean Cu particle size [c] (nm)	Metal Cu dispersion [d] D_{Cu} (%)	Surface Area of metallic Cu [e] SA_{Cu} $(m^2 \cdot g^{-1})$
Cu/MMO − S1	93.3	31.2	4.5	5.2	10.7	22.6
Cu/MMO − S2	94.2	31.8	4.9	5.6	14.0	30.1
Cu/MMO − S3	110.4	30.6	5.3	5.8	17.1	35.2
Cu/MMO − S4	74.2	30.5	6.1	7.0	12.5	25.8
Cu/MMO − S5	41.1	30.4	8.3	8.8	9.7	19.9
Cu/MgO	47.5	32.3	9.1	9.4	7.8	17.0
Cu/Al$_2$O$_3$	52.6	31.9	9.3	9.7	8.6	18.6

[a]Cu species content was measured by ICP–AES. [b]Crystallite size of Cu was calculated by the Debye-Scherrer equation based on XRD patterns.[c]Mean particle size of Cu was determined by TEM.[de]Dispersion and surface area of metallic Cu were determined according to the results of N$_2$O chemisorption and H$_2$ pulse reduction (described in Experimental Section).

3.2. Studies on Cu species and surface acid−base property

To investigate the effect of calcination temperatures on the reducibility of samples, H$_2$−TPR tests were performed and displayed in Fig. S3. All these samples display observable reduction peaks below 573 K, indicating copper species can be completely reduced at 573 K. The main reduction peaks of Cu/MMO shifts to low temperature from Cu/MMO − S1 to Cu/MMO − S3, and then moves to high temperature from Cu/MMO − S3 to Cu/MMO − S5, which shows an identical variation trend with SA$_{Cu}$ and D$_{Cu}$. In situ XPS spectra were measured to provide information on chemical state of surface copper species. The spectra of CuMgAl − MMO samples display Cu 2$p_{3/2}$ (∼933.6 eV), Cu 2$p_{1/2}$ peaks (∼953.4 eV) and several satellite peaks (Fig. S4), attributed to the characteristic peaks of Cu^{2+} species in MMO materials. After an in situ reduction treatment in a H$_2$/Ar (1/9, v/v) atmosphere at 573 K, two peaks at ∼933.0 eV and ∼953.0 eV (Fig. 3A) are observed, corresponding to Cu 2$p_{3/2}$ and Cu 2$p_{1/2}$ of Cu° and/or Cu$^+$, respectively [34]. Since these two Cu species (Cu° and Cu$^+$) have rather similar binding energies, in situ XAES measurements were performed to discriminate Cu species and the results were shown in Fig. 3B. Surprisingly, all these five Cu/MMO samples display rather close characteristic peaks centered at 918.6 eV of kinetic energy values, which is associated with Cu° species, based on a comparison with in situ Cu$_{LMM}$ XAES standard spectra peak of CuO (∼917.7 eV), Cu$_2$O (∼916.8 eV) and Cu (∼918.6 eV) (Fig. 3B). The results above confirm Cu° species is the predominant chemical state of surface copper for as-prepared Cu/MMO samples.

In situ X-ray absorption fine structure (XAFS) examinations for Cu/MMO samples at Cu K-edge under reduction conditions were performed to probe coordination environment, with Cu, Cu$_2$O and CuO as reference samples. The normalized XANES spectra at Cu K-edge of these Cu/MMO samples are quite similar to those of Cu foil (Fig. S5). Fig. 3C displays the first derivative profiles of these XANES spectra, from which the peaks with absorption edge energy at 8979.0 eV, 8980.4 eV and 8984.1 eV are attributed to Cu foil, Cu$_2$O and CuO, respectively [35–37]. It should be noted that the first derivative profiles of all these Cu/MMO samples agree well with that of Cu foil, and neither Cu$_2$O nor CuO are observed. Furthermore, the Fourier transform of k3-weighted EXAFS spectra of these Cu/MMO samples at Cu K-edge (R-space plot) and corresponding curve fitting in the R range 1–3 Å are obtained (Fig. 3D). The fitting results including bond distance, coordination number and fraction of metallic copper are listed in Table S2. The first Cu − Cu shell distance of metallic copper phase (∼2.56 Å) in Cu/MMO samples is the same to Cu foil reference (2.56 Å). In comparison with the bulk metallic Cu phase, the relative content of metallic Cu atoms in Cu/MMO samples was estimated (Table S2) [34,38]. Notably, the percentage of Cu° among all Cu species is 93.1 ± 7.5%, indicating that metallic Cu is dominant in these Cu/MMO samples. Furthermore, in situ FTIR of CO chemisorption was used to distinguish surface Cu species. The Cu/MMO − S3 sample was activated by a H$_2$/Ar (1/9, v/v)
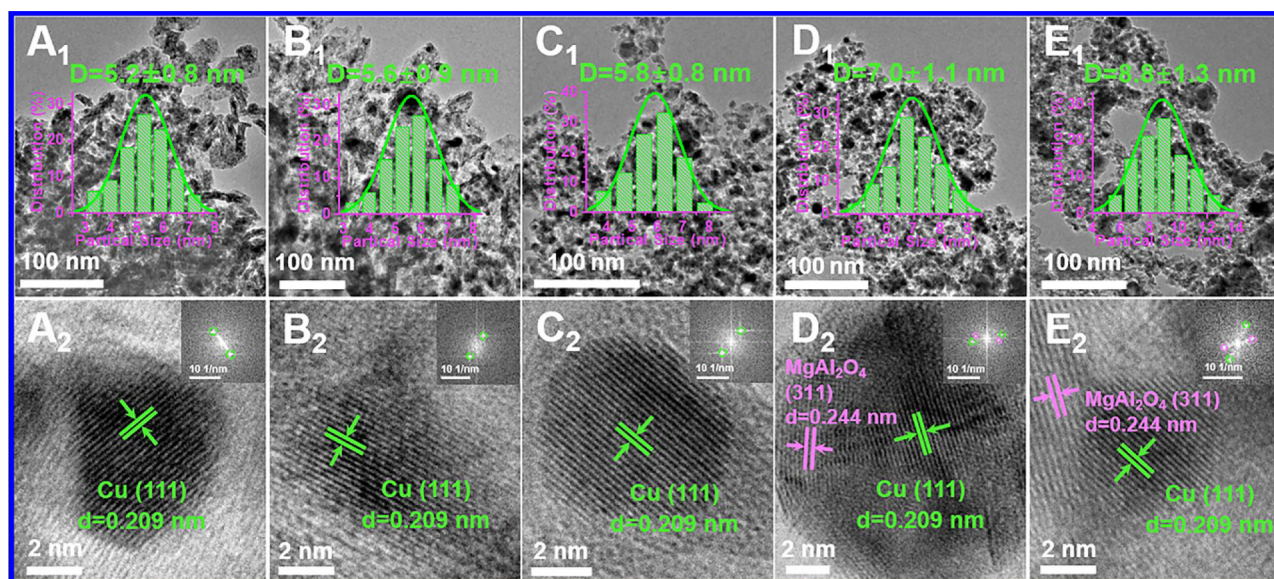

Fig. 2. HRTEM images of Cu/MMO samples: (A) Cu/MMO − S1, (B) Cu/MMO − S2, (C) Cu/MMO − S3, (D) Cu/MMO − S4, (E) Cu/MMO − S5. Inset: histogram of size distribution according to 300 counted nanoparticles (A1–E1) and corresponding FFT images (A2–E2).
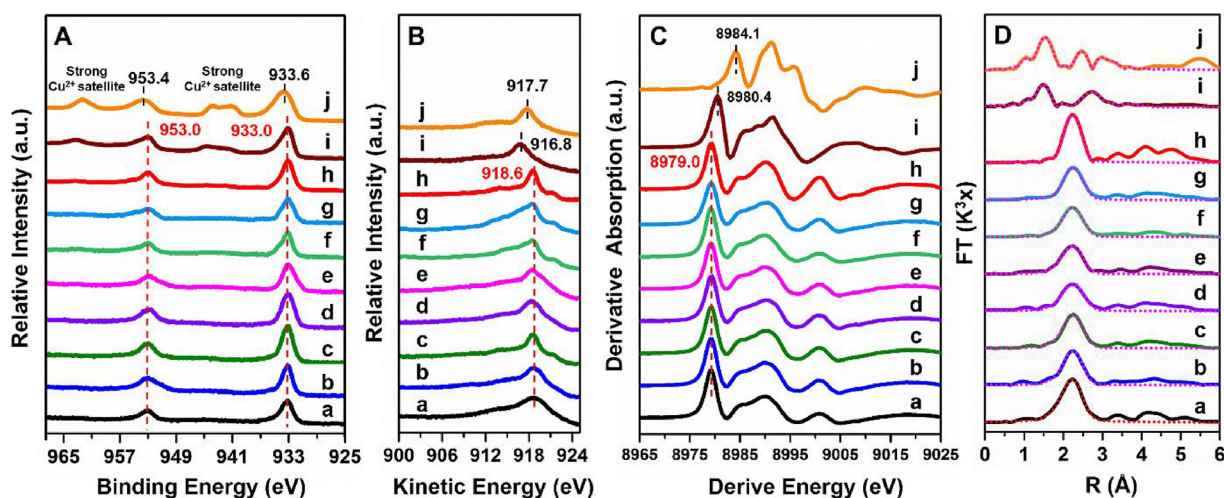
Fig. 3. (A) *In situ* XPS spectra, (B) corresponding XAES spectra, (C) the first derivative from *in situ* Cu K-edge XANES spectra and (D) Fourier-transform EXAFS spectra at Cu K-edge for Cu/MMO samples without phase corrected (the dotted line: fitting curve; the solid line: experimental data): (a) Cu/MMO − S1, (b) Cu/MMO − S2, (c) Cu/MMO − S3, (d) Cu/MMO − S4, (e) Cu/MMO − S5, (f) Cu/MgO, (g) Cu/Al$_2$O$_3$, (h) Cu foil, (i) Cu$_2$O, (j) CuO.

atmosphere at 573 K for 4 h, followed by CO adsorption at room temperature for 1.0 h. Subsequently, FTIR spectra were recorded within 2300–2000 cm^{-1} in a high purity He flow. As shown in Fig. S6, the CO bands vanish quickly after purging He from 0 to 5 min, indicating no chemisorption CO species but physical adsorption on metallic Cu$^{\circ}$ site. This is consistent with the aforementioned *in situ* studies of XRD, XPS, XAES and XAFS results.

To obtain qualitative and quantitative surface acidity of Cu/MMO samples, two kinds of experimental approaches including *in situ* FTIR of pyridine adsorption and NH$_3$ − TPD were elaborately carried out. Fig. 4A shows *in situ* Py − FTIR spectra of Cu/Al$_2$O$_3$, Cu/MgO and Cu/MMO samples toward pyridine adsorption after evacuation at 423 K within the frequency range 1700–1400 cm^{-1}. The spectrum of Cu/Al$_2$O$_3$ sample displays five bands: bands at 1450 cm^{-1} and 1610 cm^{-1} are attributed to the ν(C–H) deformation vibration and ν(C–C) vibration of pyridine adsorbed at Lewis acidic sites; bands at 1542 and 1640 cm^{-1} are generally assigned to the in-plane ring-breathing vibrations ν(CCN) of pyridine at Brønsted acidic sites (PyH$^+$); the band at 1490 cm^{-1} reflects a mixture of Brønsted acidic and Lewis acidic site toward pyridine adsorption [39,40]. In the cases of five Cu/MMO samples, characteristic bands of Lewis acid sites at 1450, 1490 and

1610 cm^{-1} are due to pyridine molecules coordinated with ν19b, ν19a and ν8a modes of ν(CCN), respectively. However, PyH$^+$ band at Brønsted acid sites is not detected. Interestingly, the Py-FTIR spectra of Cu/MMO samples are rather similar to that of Cu/MgO sample, except that the latter gives negligible bands associated with acidity. This indicates pyridine adsorption occurs on unsaturated Al^{3+} of Cu/MMOs *via* nitrogen-lone-pair electrons.

In order to further investigate the acidic strength, the FTIR spectra of Cu/MMO − S3 sample were recorded by temperature programmed desorption of pyridine until the disappearance of all bands. As shown in Fig. 4B, the Cu/MMO − S3 sample after purged at 298 K displays Lewis acid sites (1450 and 1610 cm^{-1}), hydrogen-bonded sites (1596 cm^{-1}), and physical adsorption sites (1580 cm^{-1}). All these bands decline substantially along with the increment of desorption temperature. Elevating the temperature to 423 K causes the disappearance of both bands due to physisorbed sites and hydrogen-bonded sites; while the Lewis acid bands diminish gradually and disappear at 523 K. The observations above indicate that medium-strong and weak acid sites are predominant in Cu/MMO samples. In addition, the acid strength and acid amount were determined by NH$_3$ − TPD measurements. For Cu/MgO, absorption of NH$_3$ is hardly observed. The Cu/Al$_2$O$_3$ sample
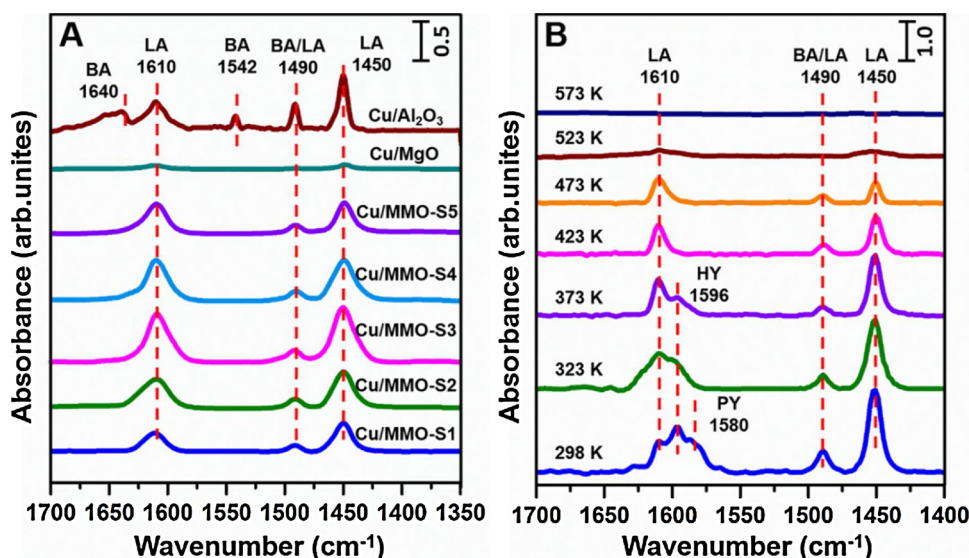

Fig. 4. (A) *In situ* FTIR spectra of pyridine on various samples at 423 K; (B) *in situ* FTIR spectra of pyridine on Cu/MMO − S3 at different temperatures.

Table 2
Catalytic Performance and Concentration of Acid and Base Site for Various Samples.

Catalyst	Cu sites	Acid Sites	Base Sites			STY_{EG} [f]	TOF
	S_{Cu}° [a] $(m^2 \cdot g^{-1})$	LA [b] $(mmol \cdot g^{-1})$	BW [c] $(mmol \cdot g^{-1})$	BM [d] $(mmol \cdot g^{-1})$	BT [e] $(mmol \cdot g^{-1})$	$(g \cdot g_{cat}^{-1} \cdot h^{-1})$	(h^{-1})
Cu/MMO − S1	22.6	0.336	0.166	0.322	0.488	0.426	18.8
Cu/MMO − S2	30.1	0.429	0.225	0.474	0.699	0.539	22.1
Cu/MMO − S3	35.2	0.463	0.262	0.521	0.783	0.602	23.6
Cu/MMO − S4	25.8	0.406	0.231	0.432	0.663	0.497	20.8
Cu/MMO − S5	19.9	0.167	0.085	0.146	0.231	0.356	16.5
Cu/MgO	17.1	0.036	0.413	0.538	0.951	0.037	3.6
Cu/Al$_2$O$_3$	18.6	0.485	0.046	0.057	0.103	0.056	5.3

[a] Surface area of metallic Cu was determined based on the results of N_2O chemisorption and H_2 pulse reduction.
[b] LA is the concentration of Lewis acid site.
[c] BW represents the concentration of weak base site.
[d] BM is the concentration of medium − strong base site.
[e] BT is the total concentration of base sites.
[f] STY_{EG} denotes the normalized space-time yield of EG.

shows two broad desorption peaks in the temperature range 390–445 K and 445–560 K (Fig. S7), which are ascribed to weak (surface OH group) and strong acid site (unsaturated Al^{3+}), corresponding to NH_3 adsorption on Brønsted acid and Lewis acid site, respectively [41]. In the cases of Cu/MMO samples, one broad desorption peak within 393–513 K is observed, which is due to NH_3 desorption from moderate Lewis acid site. The corresponding acid concentration of all samples were evaluated based on the fitted peak area (Table 2). Interestingly, the concentration of surface acid sites increases gradually from Cu/MMO − S1 to Cu/MMO − S3 but decreases from Cu/MMO − S3 to Cu/MMO − S5, and the sample of Cu/MMO − S3 presents the largest concentration of surface acid sites.

In addition to studies on acidity, the surface basicity of various samples was also determined by CO_2−TPD measurements. To acquire the distribution of basic concentration and strength, all the spectra are fitted and deconvoluted *via* a multi-peaks Gaussian fitting method (as shown in Fig. 5 and Table 2). The profile of Cu/MgO sample are deconvoluted to three peaks in the region of 413–473 K, 473–503 K,
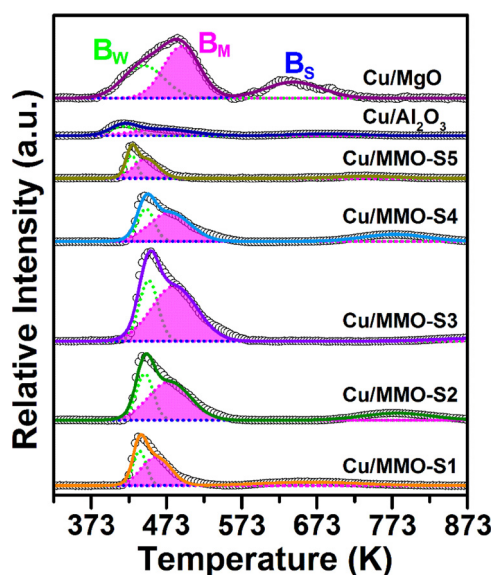

Fig. 5. CO_2−TPD profiles of various samples (the black dotted line: experimental data; the solid line: fitting curve) deconvoluted into three peaks from 323 K to 873 K: weak base site (B_W, green dotted line at the first peak region), medium-strong base site (B_M, magenta dotted line at the second peak region) and strong base site (B_S, blue dotted line at the third peak region). (For interpretation of the references to colour in this figure legend, the reader is referred to the web version of this article).
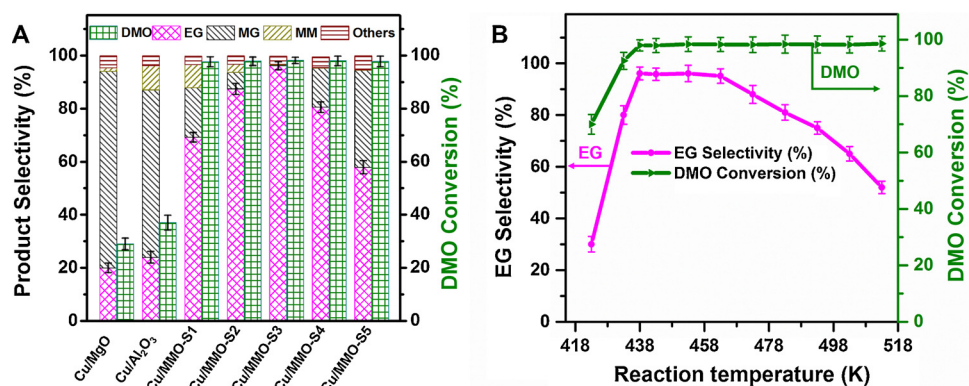
593–633 K, which are attributed to the weak (surface OH^- group), medium-strong (Mg−O−Mg group or Mg^{2+}–O^{2-} pairs) and strong base site (coordinately unsaturated O^{2-}), respectively [42]. The Cu/MMO samples display similar CO_2−TPD profile to Cu/MgO sample, with a broad peak at low temperature and a weak one at relatively high temperature. The broad one can be deconvoluted into two peaks in the region (413–473 K) and (473–503 K) ascribed to weak and medium-strong base site, corresponding to surface OH^- group and Mg−O−Mg group (or Mg^{2+}–O^{2-} pairs), respectively. Compared with Cu/MgO, the amount of strong base site of Cu/MMO samples is rather slight, possibly due to the interaction between MgO and Al_2O_3. It should be noted that from Cu/MMO − S1 to Cu/MMO − S5, the concentration of weak or medium-strength basic site increases firstly and then decreases; the sample of Cu/MMO − S3 presents the maximum value of either weak or medium basic site, in accordance with the largest concentration of surface acid sites, the highest dispersion and surface area of Cu.

3.3. Catalytic performances toward vapor-phase hydrogenation of DMO

The vapor-phase hydrogenation of dimethyl oxalate to produce ethylene glycol (DMO to EG) is a typical reaction of fatty esters with great industrial importance [5]. However, DMO hydrogenation is a rather complicated reaction involving activation of C=O/C−O bond whereas the retention of C−C bond under rigorous reaction conditions, which results in tandem reaction routes involving DMO hydrogenation to methyl glycolate (MG), MG hydrogenation to EG, and deep hydrogenation of EG to ethanol (EtOH) [43]. Thus, a highly-efficient hydrogenation of DMO to EG with low energy consumption under moderate operation conditions is extremely desirable. In this work, the vapor-phase hydrogenation reaction of DMO to produce EG was performed over these prepared Cu/MMO catalysts. Fig. 6A shows DMO conversion and products distribution over these catalysts, which are conducted under identical conditions (Temperature: 438 K; WLHSV-$_{DMO}$: 1.0 $g \cdot g_{cat}^{-1} h^{-1}$; H_2 pressure: 2.0 MPa; H_2/DMO molar ratio: 50). Notably, these five Cu/MMO catalysts derived from LDHs display a DMO conversion of ˜98.0%, which is almost up to a full DMO conversion on reported Cu catalysts (Table S3: 98%–100%) and is significantly superior to the reference samples of Cu/MgO (˜29.2%) and Cu/Al$_2$O$_3$ (˜36.9%). Interestingly, the selectivity to EG increases firstly from Cu/MMO − S1 to Cu/MMO − S3 and then decreases from Cu/MMO − S3 to Cu/MMO − S5. The highest catalytic selectivity of ˜96.1% is present in the sample of Cu/MMO − S3, far beyond that of Cu/MgO (˜19.8%) and Cu/Al$_2$O$_3$ (˜23.9%). The main by-product is MG (the intermediate product from DMO to EG), with other minor by-products (*e.g.*, methyl methoxyacetate, ethanol, 1,2-butanediol and 1,2-propylene glycol) shown in Table S4. The Cu/Al$_2$O$_3$ catalyst with acid sites induces EG

etherification to methyl methoxyacetate and 2-methoxyethanol; whereas Cu/MgO with strong basic sites results in Guerbet reaction with the formation of 1, 2-butanediol (1,2-BDO). In contrast, Cu/MMO catalyst shows a high selectivity to EG (96.1%), due to a fine control over the balance between Lewis acid and medium-strong base site *via* tuning structural transformation of LDHs precursors.

Reaction conditions would impose great influences on catalytic performance (activity, selectivity, and lifespan) [44,45]. Therefore, the catalytic performance of optimal catalyst (Cu/MMO − S3) toward DMO hydrogenation was investigated with respect to reaction temperature (Fig. 6B), pressure (Fig. S8 A), WLHSV (Fig. S8B), molar ratio of H_2/DMO (Fig. S8C), as well as particle size (Table S6), respectively, in order to eliminate influences of heat transfer, external/internal diffusion and thus achieve enhanced catalytic performance. As illustrated in Fig. 6B, the conversion of DMO increases rapidly from 423 K to 438 K (~98.0%), and remains constant in the temperature range 438–503 K. This indicates a full gasification and catalytic conversion of DMO at 438 K. The EG selectivity shows a big variation along with the increase of reaction temperature: it rises from 30.2% (at 423 K) to the maximal value of ~96.1% (at 438 K), followed by a slow decline (within 438–463 K) and then a continuous decrease (within 463–503 K). In contrast, the selectivity of EtOH as the main by-product of EG deep hydrogenation, increases as the reaction temperature rises from 453 K to 553 K, which is a typical tendency of tandem reaction. The results above show that DMO hydrogenation to EG can be facilely controlled by regulating reaction temperature over Cu/MMO − S3 catalyst: at 438 K, a DMO conversion of 98.2% and an EG selectivity of 96.1% are obtained. This is, to the best of our knowledge, the lowest reaction temperature with superior catalytic performance compared with previously reported Cu-based catalytic systems (Table S3). In order to further study intrinsic catalytic activity, turn over frequency (TOF) value was calculated at a low DMO conversion (below 20%) in Table S5. The optimal catalyst Cu/MMO − S3 in this work gives a high TOF value of 23.6 h^{-1}, which is larger than previously reported Cu-based catalysts (normally within 10–18 h^{-1} in Table S3). The long-term stability of catalyst, which is another significant parameter, was studied under the above mild condition of 438 K. As shown in Fig. S8D, DMO conversion decreases slightly from 98.2% to 96.4% and EG selectivity declines from 96.1% to 94.1% after 120 h over Cu/MMO − S3 catalyst, demonstrating a satisfactory stability. *In situ* XPS measurements over the fresh and used Cu/MMO − S3 catalyst in an on-line reaction cell were executed under the same conditions (Fig. S9A − B), both of which showed unvaried Cu 2*p* XPS and Cu LMM XAES spectra attributed to Cu° species. Moreover, during this long-term reaction, no apparent change in structure or morphology was observed *via* HRTEM for the fresh (Fig. 2C) and used Cu/MMO − S3 catalyst (Fig. S9C − D). A low reaction temperature (438 K) depresses sintering/agglomeration of copper nanoparticles and therefore improves the catalyst stability.

3.4. Studies on structure − property correlation

Normally, transition metal (Cu, Co, Ni, *etc.*) is submitted to activate hydrogen molecule in heterogeneous hydrogenation reaction. The $H_2 − TPD$ measurements over Cu/MMO catalysts were conducted to identify hydrogen surface adsorption and hydrogen dissociation on these heterogeneous catalysts. For all these Cu-based catalysts (Fig. S10), a H_2 desorption peak in a low temperature range (300–400 K) is observed, corresponding to chemical adsorption of H_2 on the surface of metallic Cu, since the sample of MgO − Al_2O_3 gives no desorption peak at all [46]. Compared with the reference samples of Cu/MgO and Cu/Al_2O_3, Cu/MMO catalysts display both increased peak intensity and integral area, indicating a significantly enhanced H_2 activation and surface concentration of H species. Furthermore, the sample of Cu/MMO − S3 exhibits the strongest peak intensity with the largest integral area, in accordance with the maximal value of D_{Cu} and SA_{Cu} in Table 1.

In order to acquire more information about chemical state of adsorbed species on catalysts, *in situ* FTIR spectroscopic technology was exploited to study the DMO adsorption (DMO dissolved in methanol) on the surface of metallic copper nanoparticles, Cu/MgO, Cu/Al_2O_3 and Cu/MMO − S3 sample, respectively. The influence of methanol on the measurement results was firstly excluded at 303 K (Fig. S11): the adsorption peaks of methanol vanished quickly after purging He within only 3 min, indicating a rather weak methanol sorption (*i.e.*, physical absorption) on Cu/MMO − S3 catalyst. Thus, the effect of solvent is negligible and would not be concerned in the following discussion. The FTIR spectra of solid DMO in the absence of catalyst were measured at 300 K (solid state) and 438 K (gaseous state), respectively, as a reference sample (Fig. 7A, a1 and a2). At 300 K, the two bands at 1740 and 1438 cm^{-1} are ascribed to $\nu(C=O)$ and $\delta_{as}(CH_3)$, respectively; and another two bands at 1210 and 1160 cm^{-1} are assigned to the split stretching vibration peak of $\nu(C–O−C)$ [47–49]. However, the spectrum of gaseous DMO (at 438 K) shows a significant change: a new band at 1328 cm^{-1} appears due to bending vibration $\delta_s(CH_3)$, and $\nu(C=O)$ band separates into two bands (centrosymmetric and asymmetry) at 1780 cm^{-1} and 1760 cm^{-1}.

Based on above results, the reactant solution (DMO dissolved in methanol) was carefully flowed into the *in situ* reaction cell at the room temperature (300 K) for 30 min, followed by purging He to remove the gaseous and weakly-adsorbed methanol and DMO. Subsequently, the reaction cell was increased to the reaction temperature (438 K) for the measurement of chemical adsorption. It should be noted that the spectrum of DMO adsorbed on Cu nanoparticles (Fig. 7A, e1) shows very weak bands at 300 K, which can not be detected as the temperature increases to 438 K (Fig. 7A, e2). This confirms that chemical adsorption of C=O/C−O would not occur on the surface of Cu° species at the reaction temperature of 438 K. However, a series of characteristic bands (C=O/C−O) of DMO are observed on the samples of Cu/MgO, Cu/Al_2O_3 and Cu/MMO − S3 at both 300 K and 438 K. In the cases of
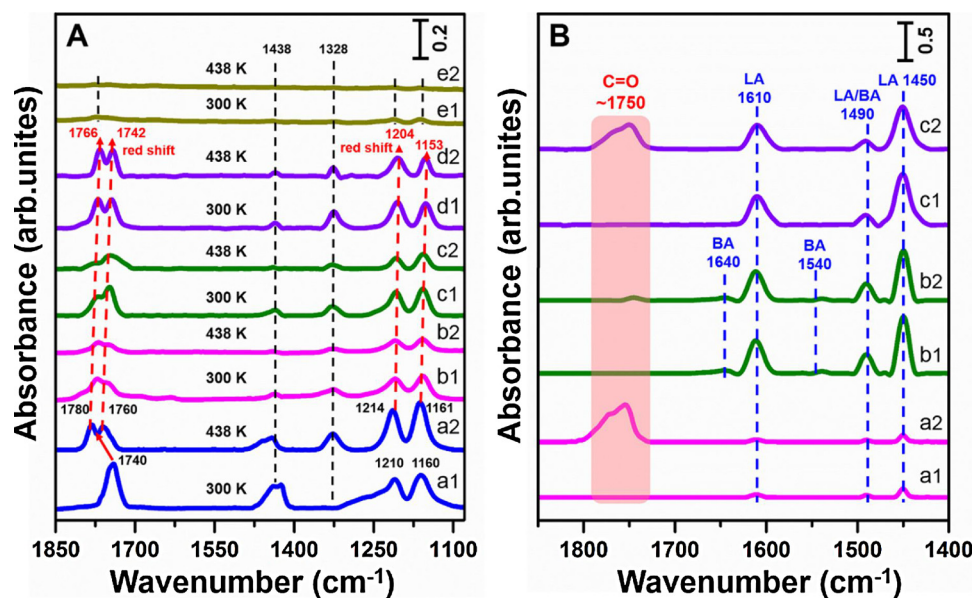
Fig. 7. (A) *In situ* FTIR spectra of DMO adsorption at room temperature 300 K and reaction temperature 438 K over various samples: (a) DMO (pure solid sample), (b) Cu/MgO, (c) Cu/Al₂O₃, (d) Cu/MMO − S3, (e) metallic nanocopper. Herein, 1 denotes at 300 K and 2 represents at 438 K. (B) *In situ* FTIR spectra of pyridine at 423 K on (a1) Cu/MgO, (b1) Cu/Al₂O₃, (c1) Cu/MMO − S3, and DMO adsorption after pyridine pretreatment on (a2) Cu/MgO, (b2) Cu/Al₂O₃, (c2) Cu/MMO − S3.

Cu/MgO (Fig. 7A, curve b) and Cu/Al₂O₃ (Fig. 7A, curve c), chemical adsorption of DMO is observed, whose characteristic bands show a similar red-shift from 1780, 1760, 1214 and 1161 cm⁻¹ (pure DMO) to about 1772, 1750, 1208 and 1157 cm⁻¹. Notably, the Cu/MMO − S3 catalyst (Fig. 7A, curve d) displays the most obvious red shift of characteristic bands at 300 K: from 1780, 1760, 1214 and 1161 cm⁻¹ for pristine DMO to 1766, 1742, 1204 and 1153 cm⁻¹ for adsorbed DMO, respectively, indicative of the strongest chemical adsorption of DMO on the surface of Cu/MMO − S3.

Interestingly, the two reference samples (Cu/MgO and Cu/Al₂O₃) have completely different support property according to CO₂ − TPD, pyridine − FTIR and NH₃ − TPD measurements: Cu/Al₂O₃ is dominated with acid sites whereas Cu/MgO sample provides basic sites. To clarify the individual function in the absorption of C=O/C−O, all the samples were first pre-treated by pyridine (poison toward acid sites), followed by the introduction of reactant DMO into reaction cell. It is a clear demonstration that pyridine adsorption on Cu/MgO (Fig. 7B, a1) samples is not observed while a strong adsorption occurs on both Cu/Al₂O₃ (Fig. 7B, b1) and Cu/MMO − S3 (Fig. 7B, c1), in accordance with the results of *in situ* Py − FTIR (Fig. 4). After pretreatment of pyridine, DMO was introduced carefully into the cell to interact with these three samples. Remarkably, a strong new band at about 1750 cm⁻¹ appears on the Cu/MgO sample (Fig. 7B, a2), which is assigned to ν(C=O) of adsorbed DMO. However, for Cu/Al₂O₃ sample, no any band of DMO is observed, except with the characteristic bands of pyridine (1450 and 1610 cm⁻¹) (Fig. 7B, b2). This suggests acid sites poisoned by pyridine cannot adsorb reactant DMO anymore. In the case of Cu/MMO − S3

sample (Fig. 7B, c2), both characteristic bands of pyridine and a new weak band assigned to DMO (at about 1750 cm⁻¹) are observed. On the basis of the FTIR study, it is proposed that acid sites of support would interact with the carbonyl oxygen of DMO whereas basic sites adsorb the carbonyl carbon. The C=O/C−O group are adsorbed on the surface acidic and basic site of Cu/MMO − S3; whereas a relatively weaker adsorption of DMO occurs on Cu/MgO or Cu/Al₂O₃ with basic or acidic site. Furthermore, upon degassing at 438 K, the adsorption bands of DMO still maintain almost unchanged on Cu/MMO − S3 catalyst; whilst those on Cu/MgO or Cu/Al₂O₃ become rather weak. This, consequently, accounts for the excellent catalytic performance of Cu/MMO − S3 at low reaction temperature of 438 K, in which appropriate acidic and basic site from support are crucial for the activation adsorption of C=O/C−O group of DMO.

To shed light on structure − property correlation for Cu/MMO catalysts, the studies on turn over frequency (TOF) value as a function of Cu° sites, acidic and basic site, will provide an in-depth understanding of active centers and their individual contribution toward the hydrogenation reaction. In this work, the TOF value from DMO to EG exhibits a convex monotonic increase rather than a linear relationship with the enhancement of surface Cu° concentration over Cu/MMO catalysts (Fig. 8A), illustrating that metallic Cu serves as an active site but not an exclusive factor to govern catalytic performance. Furthermore, it should be mentioned that the TOF value of Cu/MMO − S5 (16.5 h⁻¹) is almost 4 times larger than that of Cu/MgO (3.6 h⁻¹) or Cu/Al₂O₃ (5.3 h⁻¹), with the nearly same surface Cu concentration and particle size. This suggests that the hydrogenation activity of DMO is
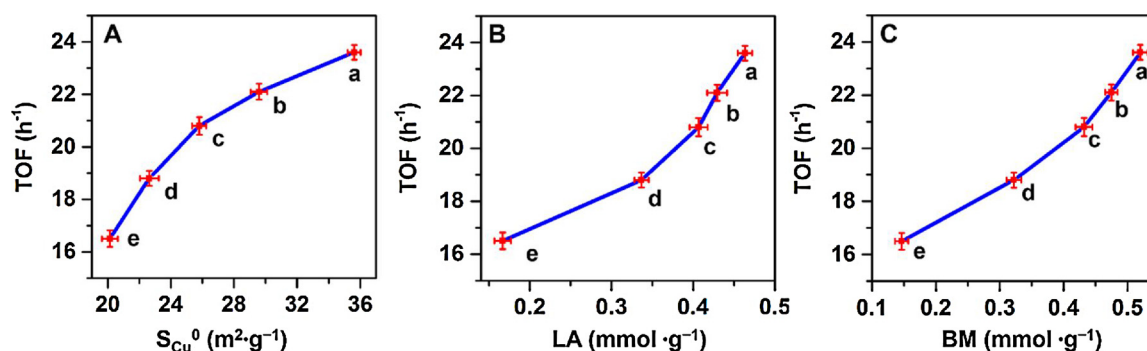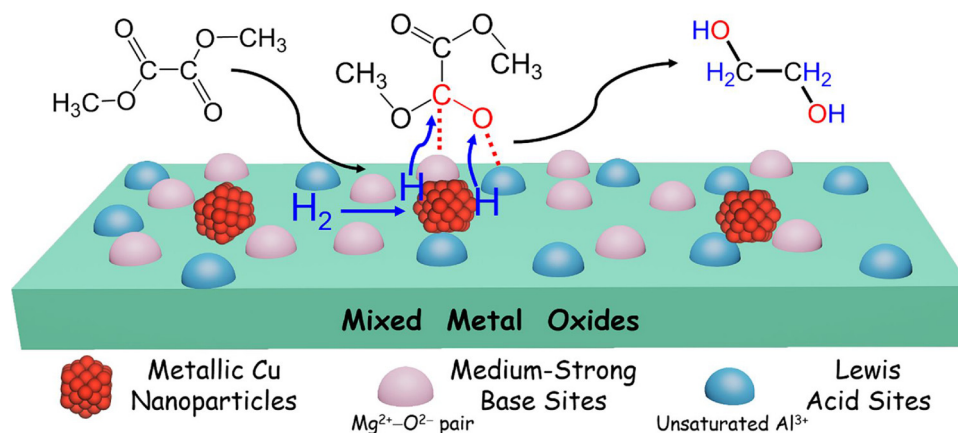

Fig. 8. Turn over frequency (TOF) as a function of surface concentration of (A) $S_{Cu}°$, (B) Lewis acid site or (C) medium-strong base site, respectively: (a) Cu/MMO − S3, (b) Cu/MMO − S2, (c) Cu/MMO − S4, (d) Cu/MMO − S1, (e) Cu/MMO − S5.

Scheme 2. Proposed ternary synergistic catalysis of DMO hydrogenation over the Cu/MMO catalyst.

not only associated with the surface Cu° species, but also related to the acid − base sites of supports. Thus, the correlation between TOF value and concentration of acidic site or basic site (Table 2) was further studied and illustrated in Fig. 8B and C. A concave monotonic increment correlation between TOF value and Lewis acid or medium-strong base concentration is observed, but no relationship is found between TOF value and weak base or total base sites. This manifests that both Lewis acid and medium-strong base site serve as active center and make a contribution to reaction process, other than weak base or total base sites. The results above substantiate that a synergistic catalysis of Cu°, Lewis acid and medium-strong base site plays a vital role in DMO hydrogenation reaction at 438 K. Remarkably, the Cu/MMO − S3 catalyst possesses the largest concentration of surface Cu° species, acidic and medium-strong basic site among all these Cu/MMO samples, accounting for the largest STY and TOF value from DMO to EG.

Although several previous studies have reported that a synergistic effect between Cu^+ and Cu° is crucial for DMO conversion to EG in Cu/SiO_2 catalytic systems, this phenomenon is absent in this work. Based on the various *in situ* investigations above and the results of previous studies, a possible synergistic catalysis process (Scheme 2) for DMO hydrogenation reaction over Cu/MMO − S3 catalyst is tentatively proposed to rationalize the structure–property correlation. Initially, the surface Cu° species serves as active site toward dissociation adsorption of hydrogen to active hydrogen atoms. In the second step, the surface Lewis acidic site (Al^{3+}) of Cu/MMO − S3 adsorbs and polarizes the oxygen atom in ester group (O=C−O) with p−π-conjugated effect; meanwhile, the medium-strong basic site ($Mg^{2+} − O^{2-}$ pair) is prone to interact with the π* acceptor orbital of ester group (C=O/C − O) at carbon atom, which thus promotes the activation adsorption of C=O/C − O bond in DMO molecule. Consequently, this ternary cooperative catalysis between Cu° species and acid − base sites facilitates the activation adsorption of DMO and subsequent hydrogenation reaction, responsible for the superior catalytic performance at a low temperature of 438 K.

4. Conclusions

In summary, we prepared a new Cu/MMO catalyst with unique ternary synergistic catalysis of Cu and acid − base sites *via* an elaborate control over topotactic structure transformation from CuMgAl − LDH precursors, which showed remarkable catalytic performance toward DMO vapor-phase hydrogenation to EG at a rather low temperature (438 K). A combination study based on a series of *in situ* characterization methods (XRD, XPS, XAFS and FTIR) reveals that the Lewis acid (Al^{3+}) and medium-strong base ($Mg^{2+} − O^{2-}$ pair) sites of support serve as active sites for adsorption of polarized C=O/C−O group while H_2 molecule undergoes dissociation adsorption on Cu° sites. The cooperative catalysis of Cu°/acid − base sites is responsible for the

excellent reaction activity at such a low temperature. These insights into the metal-support synergistic catalysis demonstrated in this work give helpful instructions for the design of heterogeneous catalysts used in other hydrogenation reactions of fatty esters.

Appendix A. Supplementary data

Supplementary material related to this article can be found, in the online version, at doi:https://doi.org/10.1016/j.apcatb.2019.02.042.

References

[1] C. Higman, S. Tam, Advances in coal gasification, hydrogenation, and gas treating for the production of chemicals and fuels, Chem. Rev. 114 (2014) 1673–1708.
[2] R. Pruett, Catalysis in C1 chemistry, Organometallics 3 (1984) 339–340.
[3] L.L. Zhong, F. Yu, Y.L. An, Y.H. Zhao, Y.H. Sun, Z.J. Li, T.J. Lin, Y.J. Lin, X.Z. Qi, Y.Y. Dai, L. Gu, J.S. Hu, S.F. Jin, Q. Shen, H. Wang, Cobalt carbide Nano prisms for direct production of lower olefins from syngas, Nature 538 (2016) 84.
[4] G. Prieto, S. Beijer, M.L. Smith, M. He, Y. Au, Z. Wang, D.A. Bruce, K.P. de Jong, J.J. Spivey, P.E. de Jongh, Design and synthesis of copper–cobalt catalysts for the selective conversion of synthesis gas to ethanol and higher alcohols, Angew. Chem. Int. Ed. 53 (2014) 6397–6401.
[5] H.R. Yue, Y.J. Zhao, X.B. Ma, J.L. Gong, Ethylene glycol: properties, synthesis, and applications, Chem. Soc. Rev. 41 (2012) 4218–4244.
[6] C. Wen, Y. Cui, X. Chen, B. Zong, W.-L. Dai, Reaction temperature controlled selective hydrogenation of dimethyl oxalate to methyl glycolate and ethylene glycol over copper-hydroxyapatite catalysts, Appl. Catal. B Environ. 162 (2015) 483–493.
[7] L.R. Zehner, R.W. Lenton, Process for the Preparation of Ethylene Glycol, US, U.S. (1976).
[8] L.F. Chen, P.J. Guo, M.H. Qiao, S.R. Yan, H.X. Li, W. Shen, H.L. Xu, K.N. Fan, Cu/SiO₂ catalysts prepared by the ammonia-evaporation method: texture, structure, and catalytic performance in hydrogenation of dimethyl oxalate to ethylene glycol, J. Catal. 257 (2008) 172–180.
[9] H. Adkins, B. Wojcik, L.W. Covert, The catalytic hydrogenation of esters to alcohols, III, J. Am. Chem. Soc. 55 (1933) 1669–1676.
[10] H.R. Yue, Y.J. Zhao, S. Zhao, B. Wang, X.B. Ma, J.L. Gong, A copper-phyllosilicate core-sheath Nano reactor for carbon–oxygen hydrogenolysis reactions, Nat. Commun. 4 (2013) 2339.
[11] S. Kattel, P.J. Ramírez, J.G. Chen, J.A. Rodriguez, P. Liu, Active sites for CO₂ hydrogenation to methanol on Cu/ZnO catalysts, Science 355 (2017) 1296–1299.
[12] S.H. Zhu, X.Q. Gao, Y.L. Zhu, Y.F. Zhu, H.Y. Zheng, Y.W. Li, Promoting effect of boron oxide on Cu/SiO₂ catalyst for glycerol hydrogenolysis to 1,2-propanediol, J. Catal. 303 (2013) 70–79.
[13] Z.Q. Wang, Z.N. Xu, S.Y. Peng, M.J. Zhang, G. Lu, Q.S. Chen, Y. Chen, G.C. Guo, High-performance and long-lived Cu/SiO₂ nanocatalyst for CO₂ hydrogenation,

ACS Catal. 5 (2015) 4255–4259.

[14] J.L. Gong, H.R. Yue, Y.J. Zhao, S. Zhao, L. Zhao, J. Lv, S.P. Wang, X.B. Ma, Synthesis of ethanol via syngas on Cu/SiO2 catalysts with balanced Cu°-Cu$^+$ sites, J. Am. Chem. Soc. 134 (2012) 13922–13925.

[15] Y. Wang, Y.L. Shen, Y.J. Zhao, J. Lv, S.P. Wang, X.B. Ma, Insight into the balancing effect of active Cu species for hydrogenation of carbon–oxygen bonds, ACS Catal. 5 (2015) 6200–6208.

[16] Z. He, H.Q. Lin, P. He, Y.Z. Yuan, Effect of boric oxide doping on the stability and activity of a Cu–SiO2 catalyst for vapor-phase hydrogenation of dimethyl oxalate to ethylene glycol, J. Catal. 277 (2011) 54–63.

[17] Y. Huang, H. Ariga, X.L. Zheng, X.P. Duan, S. Takakusagi, K. Asakura, Y.Z. Yuan, Silver-modulated SiO2-supported copper catalysts for selective hydrogenation of dimethyl oxalate to ethylene glycol, J. Catal. 307 (2013) 74–83.

[18] X.L. Zheng, H.Q. Lin, J.W. Zheng, X.P. Duan, Y.Z. Yuan, Lanthanum oxide-modified Cu/SiO2 as a high-performance catalyst for chemoselective hydrogenation of dimethyl oxalate to ethylene glycol, ACS Catal. 3 (2013) 2738–2749.

[19] X.P. Kong, X.C. Zhang, J.G. Chen, Highly active and selective CoCu/ZnO catalysts prepared by mild oxalic acid co-precipitation method in dimethyl oxalate hydrogenation, Catal. Commun. 65 (2015) 46–50.

[20] Y.N. Wang, X.P. Duan, J.W. Zheng, H.Q. Lin, Y.Z. Yuan, H. Ariga, S. Takakusagi, K. Asakura, Remarkable enhancement of Cu catalyst activity in hydrogenation of dimethyl oxalate to ethylene glycol using gold, Catal. Sci. Technol. 2 (2012) 1637–1639.

[21] R.P. Ye, L. Lin, J.X. Yang, M.L. Sun, F. Li, B. Li, Y.G. Yao, A new low-cost and effective method for enhancing the catalytic performance of Cu–SiO2 catalysts for the synthesis of ethylene glycol via the vapor-phase hydrogenation of dimethyl oxalate by coating the catalysts with dextrin, J. Catal. 350 (2017) 122–132.

[22] H.W. Liu, Q. Hu, G.L. Fan, L. Yang, F. Li, Surface synergistic effect in well-dispersed Cu/MgO catalysts for highly efficient vapor-phase hydrogenation of carbonyl compounds, Catal. Sci. Technol. 5 (2015) 3960–3969.

[23] B.M. Murphy, M.P. Letterio, B.J. Xu, Catalytic dehydration of methyl lactate: reaction mechanism and selectivity control, J. Catal. 339 (2016) 21–30.

[24] X. Jin, J. Shen, W.J. Yan, M. Zhao, P.S. Thapa, B. Subramaniam, R.V. Chaudhari, Sorbitol hydrogenolysis over hybrid Cu/CaO-Al2O3 catalysts: tunable activity and selectivity with solid base incorporation, ACS Catal. 5 (2015) 6545–6558.

[25] J. Kuljiraseth, A. Wangriya, J.M.C. Malones, W. Klysubun, S. Jitkarnka, Synthesis and Characterization of AMO LDH-derived mixed oxides with various Mg/Al ratios as acid–basic catalysts for Esterification of benzoic acid with 2-ethylhexanol, Appl. Catal., B Environ. (2018).

[26] S. He, C.M. Li, H. Chen, D.S. Su, B.S. Zhang, X.Z. Cao, B.Y. Wang, M. Wei, D.G. Evans, X. Duan, A Surface defect-promoted Ni nanocatalyst with simultaneously enhanced activity and stability, Chem. Mater. 25 (2013) 1040–1046.

[27] Q. Wang, D. O'Hare, Recent advances in the synthesis and application of layered double hydroxide (LDH) nanosheets, Chem. Rev. 112 (2012) 4124–4155.

[28] G.L. Fan, F. Li, D.G. Evans, X. Duan, Catalytic applications of layered double hydroxides: recent advances and perspectives, Chem. Soc. Rev. 43 (2014) 7040–7066.

[29] H. Chen, S. He, M. Xu, M. Wei, D.G. Evans, X. Duan, Promoted synergic catalysis between metal Ni and acid–Base sites toward oxidant-free dehydrogenation of alcohols, ACS Catal. 7 (2017) 2735–2743.

[30] Y. Zhao, F. Li, R. Zhang, David G. Evans, X. Duan, Preparation of layered double-hydroxide nanomaterials with a uniform crystallite size using a new method involving separate nucleation and aging steps, Chem. Mater. 14 (2006) 4286–4291.

[31] G.C. Chinchen, C.M. Hay, H.D. Vandervell, K.C. Waugh, The measurement of copper surface areas by reactive frontal chromatography, J. Catal. 103 (1987) 79–86.

[32] G.Q. Cui, F. Wang, S. He, M. Wei, Catalytic performance of layered double hydroxide nanosheets toward phenol hydroxylation, RSC Adv. 6 (2016) 105406–105411.

[33] J.J. Bravosuárez, B. Subramaniam, R.V. Chaudhari, Ultraviolet–visible spectroscopy and temperature-programmed techniques as tools for structural characterization of Cu in CuMgAlO$_x$ mixed metal oxides, J. Phys. Chem. C 116 (2012) 18207–18221.

[34] H.H. Yang, Y.Y. Chen, X.J. Cui, G.F. Wang, Y.L. Cen, T.S. Deng, W.J. Yan, J. Gao, S.H. Zhu, U. Olsbye, J.G. Wang, W.B. Fan, A highly stable copper-based catalyst for clarifying the catalytic roles of Cu° and Cu$^+$ species in methanol dehydrogenation, Angew. Chem. Int. Ed. 57 (2018) 1836–1840.

[35] J. Teržan, P. Djinović, J. Zavašnik, I. Arčon, G. Žerjav, M. Spreitzer, A. Pintar, Alkali and earth alkali modified CuOx/SiO2 catalysts for propylene partial oxidation: what determines the selectivity? Appl. Catal. B Environ. 237 (2018) 214–227.

[36] Y. Zhu, X. Kong, S. Zhu, F. Dong, H. Zheng, Y. Zhu, Y.-W. Li, Construction of Cu/ZrO2/Al2O3 composites for ethanol synthesis: synergies of ternary sites for cascade reaction, Appl. Catal., B Environ. (2015) 166–167 551-559.

[37] M. Tamura, T. Kitanaka, Y. Nakagawa, K. Tomishige, Cu sub-nanoparticles on Cu/CeO2 as an effective catalyst for methanol synthesis from organic carbonate by hydrogenation, ACS Catal. 6 (2016) 376–380.

[38] I. Ro, Y. Liu, M.R. Ball, D.H.K. Jackson, J.P. Chada, C. Sener, T.F. Kuech, R.J. Madon, G.W. Huber, J.A. Dumesic, Role of the Cu-ZrO2 interfacial sites for conversion of ethanol to ethyl acetate and synthesis of methanol from CO2 and H2, ACS Catal. 6 (2016) 7040–7050.

[39] E.P. Parry, An infrared study of pyridine adsorbed on acidic solids. Characterization of surface acidity, J. Catal. 2 (1963) 371–379.

[40] V.M. Benítez, J.C. Yori, C.R. Vera, C.L. Pieck, J.M.G. And, J.M. Parera, Characterization of transition-metal oxides promoted with Oxoanions by means of test reactions, Ind. Eng. Chem. Res. 44 (2005) 1716–1721.

[41] J.S. Valente, E. Lima, J.A. Toledoantonio, M.A. Cortesjacome, L. Lartundorojas, R. Montiel, J. Prince, Comprehending the thermal decomposition and reconstruction process of Sol–Gel MgAl layered double hydroxides, J. Phys. Chem. C 114 (2010) 2089–2099.

[42] D. Li, R. Li, M. Lu, X. Lin, Y. Zhan, L. Jiang, Carbon dioxide reforming of methane over Ru catalysts supported on Mg-Al oxides: a highly dispersed and stable Ru/Mg (Al)O catalyst, Appl. Catal. B Environ. 200 (2017) 566–577.

[43] Y.F. Zhu, X. Kong, X.Q. Li, G.Q. Ding, Y.L. Zhu, Y.W. Li, Cu nanoparticles inlaid mesoporous Al2O3 As a high-performance bifunctional catalyst for ethanol synthesis via dimethyl oxalate hydrogenation, ACS Catal. 4 (2014) 3612–3620.

[44] Y.T. Liu, J. Ding, J.Q. Sun, J. Zhang, J.C. Bi, K.F. Liu, F.H. Kong, H.C. Xiao, Y.P. Sun, J.G. Chen, Molybdenum carbide as an efficient catalyst for low-temperature hydrogenation of dimethyl oxalate, Chem. Commun. (Camb.) 52 (2016) 5030–5032.

[45] D.W. Yao, Y. Wang, Y. Li, Y.J. Zhao, J. Lv, X.B. Ma, A high-performance nanoreactor for carbon–oxygen bond hydrogenation reactions achieved by the morphology of nanotube-assembled hollow spheres, ACS Catal. 8 (2017) 1218–1226.

[46] H.J. Wan, B.S. Wu, H.W. Xiang, Y.W. Li, Fischer–Tropsch synthesis: influence of support incorporation manner on metal dispersion, metal–support interaction, and activities of iron catalysts, ACS Catal. 2 (2012) 1877–1883.

[47] C.Z. Wang, P.J. Chen, Y.K. Li, G.F. Zhao, Y. Liu, Y. Lu, In situ DRIFTS study of CO coupling to dimethyl oxalate over structured Al-fiber@ns-AlOOH@Pd catalyst, J. Catal. 344 (2016) 173–183.

[48] B.J. Bulkin, The infrared spectra of complex molecules, J. Polym. Sci. Part A: Polym. Chem. 19 (1981) 520-520.

[49] S. Hegde, K. Tharpa, S.R. Akuri, K. Rakesh, A. Kumar, R. Deshpande, S.A. Nair, In situ spectroscopic studies on vapor phase catalytic decomposition of dimethyl oxalate, Phys. Chem. Chem. Phys. 19 (2017) 8034–8045.